Systems/Circuits

Action Potential Generation in an Anatomically Constrained Model of Medial Superior Olive Axons

Simon Lehnert,[1] Marc C. Ford,[1,2] Olga Alexandrova,[1] Franziska Hellmundt,[1,2] Felix Felmy,[1,3] Benedikt Grothe,[1] and Christian Leibold[1]

[1]Department Biology II, [2]Graduate School of Systemic Neurosciences, and [3]Department Biology I, BioImaging Zentrum, Ludwig-Maximilians-Universität München, D-82152 Planegg-Martinsried, Germany

Neurons in the medial superior olive (MSO) encode interaural time differences (ITDs) with sustained firing rates of >100 Hz. They are able to generate such high firing rates for several hundred milliseconds despite their extremely low-input resistances of only few megaohms and high synaptic conductances *in vivo*. The biophysical mechanisms by which these leaky neurons maintain their excitability are not understood. Since action potentials (APs) are usually assumed to be generated in the axon initial segment (AIS), we analyzed anatomical data of proximal MSO axons in Mongolian gerbils and found that the axon diameter is <1 μm and the internode length is ~100 μm. Using a morphologically constrained computational model of the MSO axon, we show that these thin axons facilitate the excitability of the AIS. However, for ongoing high rates of synaptic inputs the model generates a substantial fraction of APs in its nodes of Ranvier. These distally initiated APs are mediated by a spatial gradient of sodium channel inactivation and a strong somatic current sink. The model also predicts that distal AP initiation increases the dynamic range of the rate code for ITDs.

Key words: **action potential; axon; coincidence detection; interaural time difference; sound localization**

Introduction

The generation of action potentials (APs) is widely assumed to take place in the axon initial segment (AIS). Evidence for this assumption stems predominantly from cortical pyramidal neurons and cerebellar Purkinje neurons using simultaneous somatic and axonal whole-cell recordings (Stuart and Sakmann, 1994; Stuart et al., 1997; Kole et al., 2007; Shu et al., 2007) and voltage-sensitive dye imaging (Palmer and Stuart, 2006; Foust et al., 2010; Palmer et al., 2010; Popovic et al., 2011). At rest, these neurons have relatively high input resistances of 10–200 MΩ, allowing them to integrate synaptic inputs over several milliseconds. Thus, during depolarizing stimuli, the soma generally serves as a strong and temporarily stable current source for the AIS. In neurons with very low input resistances of 2–5 MΩ, the mechanisms of AP initiation have not yet been studied in such great detail. In those cells, the membrane time constants are too short to allow the soma to serve as a temporarily stable current source. Conversely, the soma might even act as a current sink to the AP generating zone and therefore increases the AP threshold at the AIS.

In the present study, we investigated AP generation in neurons of very low input resistance, the principal cells of the medial superior olive (MSO). These neurons have membrane time constants in the range of only a few hundreds of microseconds and input resistances as low as 5 MΩ (Scott et al., 2005; Couchman et al., 2010). The MSO is a binaural nucleus in the ascending auditory pathway. MSO neurons encode the azimuthal position of low-frequency sounds via differences in the time of arrival at the two ears by their firing rate (Goldberg and Brown, 1969; Yin and Chan, 1990; Fitzpatrick et al., 1997; Brand et al., 2002) with a precision of only a few tens of microseconds. This exquisite temporal precision of binaural coincidence detection is partly achieved by the fast membrane time constants of neurons resulting from the high expression of low-voltage-activated potassium channels and hyperpolarization-activated cation channels (Svirskis et al., 2002; Koch et al., 2004; Scott et al., 2005; Mathews et al., 2010; Baumann et al., 2013), both of which are already open at rest. Despite the resulting low input resistance, these neurons can fire at high rates of ~100 Hz and more. The mechanisms by which this is possible are still unresolved.

In this article, we address the question of how AP generation is accomplished in leaky neurons using a computational model of MSO neurons with axonal morphology based on new detailed morphometric data. Our simulations show that, despite the leaky soma, the AIS remains electrotonically isolated and retains its ability to generate APs. However, we also identified conditions under which the APs are initiated at the nodes of Ranvier. This distal initiation of APs increases the dynamic range of the rate code of interaural time differences (ITDs).

Received Sept. 20, 2013; revised March 5, 2014; accepted March 8, 2014.

Author contributions: S.L., M.C.F., O.A., F.F., B.G., and C.L. designed research; S.L., M.C.F., O.A., F.H., and F.F. performed research; S.L., M.C.F., O.A., F.H., and F.F. analyzed data; S.L., M.C.F., F.F., B.G., and C.L. wrote the paper.

This work was supported by the German Research Foundation via the Collaborative Research Center 870 and the Elisabeth und Helmut Uhl Stiftung.

The authors declare no competing financial interests.

Correspondence should be addressed to Christian Leibold, Computational Neuroscience, Department Biology II, Ludwig-Maximilians-University Munich, Grosshaderner Strasse 2, D-82152 Planegg-Martinsried, Germany. E-mail: leibold@bio.lmu.de.

DOI:10.1523/JNEUROSCI.4038-13.2014

 0270-6474/14/345370-15$15.00/0

Materials and Methods

General

All experiments were performed according to institutional guidelines, and national and regional laws; it was approved by the Regierung von Oberbayern (AZ55.2–1-54–2531-105–10). All results are given as the mean ± SEM.

Retrograde labeling of MSO cells

Mongolian gerbils (*Meriones unguiculatus*) of either sex [$n = 4$; postnatal day 29 (P29) to P31] were anesthetized with pentobarbital (2 mg/kg body weight) and intracardially perfused with ice-cold Ringer's solution containing 0.1% heparin. After decapitation, the brainstem was removed from the skull under ice-cold dissection solution comprising the following (in mM): 125 NaCl, 2.5 KCl, 1 $MgCl_2$, 0.1 $CaCl_2$, 25 glucose, 1.25 NaH_2PO_4, 25 $NaHCO_3$, 0.4 ascorbic acid, 3 *myo*-inositol, and 2 pyruvic acid (all chemicals were from Sigma-Aldrich). For retrograde labeling of MSO cells, the brainstem was sectioned along the posterior–anterior axis until the MSO, lateral superior olive, and superior paraolivary nucleus (SPN) were clearly visible. Borosilicate glass micropipettes with a tip diameter of 10–15 μm were filled with a 10% solution of tetramethylrhodamine dextran (3000 molecular weight; Invitrogen) and visually guided to the SPN. Cells were labeled by applying 2–4 electroporation pulse trains (50 ms, 50 V, 10 Hz; modified from previous studies; Ford et al., 2009). Subsequently, the explants were transferred to a chamber containing oxygenated incubation solution (same as incubation solution, but containing 2 mM instead of 0.1 mM $CaCl_2$) and incubated at room temperature for 90 min. Thereafter, brainstems were immersion fixed at room temperature overnight in 4% paraformaldehyde solution.

Immunohistochemistry

Brainstems were sectioned transversally (80–120 μm slice thickness), rinsed in PBS, and transferred to blocking solution containing 1% bovine serum albumin, 2% Triton X-100, and 0.1% saponin in PBS. Multiple-immunofluorescence labeling was performed with the following primary antibodies: ankyrin G (sc-28561; rabbit; 1:500; Santa Cruz Biotechnology), Kv1.2 (75-008 clone K14/16; mouse; 1:500; NeuroMab), microtubule-associated protein 2 (CH22103; chicken polyclonal; 1:1000; Neuromics), and myelin basic protein (ab7349; rat monoclonal; 1:20; abcam). The incubation time (4°C) for primary antibodies was 3 d. After incubation with secondary antibodies (1–2 d; 4°C) and rinsing in PBS, sections were mounted with Vectashield mounting medium.

Confocal microscopy

Confocal images were acquired with a TCS SP5-2 confocal laser-scanning microscope (Leica Microsystems) equipped with HCX PL APO 63×/numerical aperture 1.3 glycerol objective. Fluorochromes were excited at 405, 488, 561, 594, and 633 nm for aminoethylcoumarin acetate, DyLight488, tetramethylrhodamine dextran, Alexa Fluor 594, and DyLight649, respectively. The emission filters for these fluorochromes were set to (in the same order) 410–460, 510–550, 565–585, 605–625, and 640–760 nm. For each optical section the images were collected sequentially for four to five fluorochromes. Stacks of 8-bit grayscale images were obtained with axial distances of 290 nm between optical sections and a pixel size of 120.4 nm. To obtain an improved signal-to-noise ratio, each section image was averaged from five successive scans. After stack acquisition, the Z chromatic shift between color channels was corrected. RGB stacks, montages of RGB optical sections, and maximum-intensity projections were assembled into tables by using ImageJ 1.37k plugins and Photoshop version 8.0.1 (Adobe Systems) software.

Morphometry

Morphometric measurements were made from overlapping image stacks of MSO principal cells. Using the ImageJ 1.37k paint-brush tool, individual axons of MSO cells filled with tetrametylrhodamine dextran were manually labeled by following single axons subsequently through each optical section of the confocal stack (Werthat et al., 2008; for dendrites, see Couchman et al., 2010). Afterward, the neighboring axons were digitally deleted. We refer to this method as digital extraction. The same axon was identified in the neighboring overlapping confocal stacks and digitally extracted. AISs and nodes of Ranvier were identified on the basis ankyrin G/Kv1.2 antibody staining. AIS and internode lengths were measured in three dimensions in confocal stack images using the ImageJ 1.37k Sync Measure 3D tool. AIS and internodal axon diameters were measured at the positions defined by ankyrin G and Kv1.2 labeling (see Fig. 2*B*) in maximum-intensity projections of image stacks based on tetrametylrhodamine dextran labeling. The mean diameter of the first internode was averaged from measurements at several (10–29) different positions between the outer borders of the juxtaparanodes (see Fig. 2*B*, K3 and K6).

Electrophysiology

Experimental procedures were as described in Couchman et al. (2010). In brief, Mongolian gerbils of either sex of P60–P80 were anesthetized with isoflurane. Brains were removed after decapitation, and 110-μm-thick horizontal brainstem slices were taken with a VT1200S vibratome (Leica) in dissection solution containing the following (in mM): 50 sucrose, 25 NaCl, 27 $NaHCO_3$, 2.5 KCl, 1.25 NaH_2PO_4, 3 $MgCl_2$, 0.1 $CaCl_2$, 25 glucose, 0.4 ascorbic acid, 3 myo-inositol, and 2 Na-pyruvate, pH 7.4 when bubbled with 95% O_2 and 5% CO_2. Slices were incubated in recording solution (same as slice solution but with 125 mM NaCl, no sucrose, and 2 mM $CaCl_2$ and 1 mM $MgCl_2$) at 36°C for 45 min, bubbled with 5% CO_2 and 95% O_2.

Incubated slices were placed into a recoding chamber attached to a BX51WI microscope (Olympus) equipped with a custom-made gradient contrast illumination and continuously perfused with recording solution kept at 34–36°C by a Warner Instruments heating system. MSO neurons were visualized at 60× magnification with a Retiga 2000 DC camera (Till Photonics/FEI Munich). Current-clamp whole-cell recordings were performed using an EPC10/2 amplifier (HEKA Elektronik) on visually identified MSO neurons with electrode resistances of ~3 MΩ. Access resistance was estimated in voltage-clamp after break in and was bridge balanced to 100% in current-clamp mode. The internal recording solution consisted of the following (in mM): 145 K-gluconate, 4.5 KCl, 15 HEPES, 2 Mg-ATP, 2 K-ATP, 0.3 Na_2-GTP, 7.5 Na_2-phosphocreatine, 5 K-EGTA, pH 7.2. The liquid junction potential was corrected on-line with an estimated value of 17 mV.

Computational modeling

Based on the morphometric analysis, a multicompartmental model was created to study the generation of APs in MSO principal cells. The model consists of one large somatic compartment that combines the somatic and dendritic membrane surface (Ashida et al., 2007). The model focuses on the axonal morphology, since APs are generally assumed to be generated there. The axon model consisted of an unmyelinated AIS followed by an extensive myelinated part that was periodically interrupted by 21 nodes of Ranvier. Figure 1*A* shows a schematic drawing of the first segments of the model up to the fourth node of Ranvier (R4). The AIS was further subdivided into a tapering part (tAIS) and a constant part (cAIS), resembling the actual geometry of the AIS. The voltages of the compartments followed a Hodgkin–Huxley-type equation as follows:

$$C_m \frac{dV}{dt} = -(I_{\mathrm{Na}} + I_{\mathrm{KHT}} + I_{\mathrm{KLT}} + I_h + I_{\mathrm{lk}} + I_{\mathrm{syn}} + I_{\mathrm{axial}} + I_{\mathrm{ext}}),$$

where I_{ext} is the external current, and the ohmic transmembrane currents are as follows:

$$I_x(V) = g_x a_x^m b_x^n (V - E_x).$$

Here, C_m is the membrane capacitance, g_x is respective peak conductances, a_x and b_x are the gating variables, and m and n are the respective cooperativities. The dynamics of the gating variables are modeled according to first-order kinetics, as follows:

$$\frac{da}{dt} = \frac{a_\infty - a}{\tau_a} \text{ and } \frac{db}{dt} = \frac{b_\infty - b}{\tau_b}$$

where a_∞ and b_∞ are the steady-state activation functions, and τ_a and τ_b are the voltage-dependent time constants.

The axial current for the ith compartment is defined as follows:

$$I^{i}_{\text{axial}} = \frac{V_{i-1} - V_i}{R^{i-1,\,i}_{\text{axial}}} + \frac{V_{i+1} - V_i}{R^{i+1,\,i}_{\text{axial}}},$$

in which R_{axial} denotes the axial resistance between the ith compartment and its respective neighboring compartments. The axial resistance results from the geometry of the axonal segment (diameter and length) as well as the specific axial resistivity of 100 Ωcm, which is in the range of usually assumed values (Mainen et al., 1995; Mainen and Sejnowski, 1996; Shu et al., 2007).

The specific model for the sodium channel was taken from Scott et al. (2010) with a reversal potential for sodium of 69 mV and a modified conductance density in the axon of 4 nS/μm^2 to fit the firing threshold of our current-clamp measurements (see Fig. 4). We chose the somatic sodium conductance density to be 0.2 nS/μm^2, a value 20-fold smaller than that in the axon and reflecting the low sodium channel density found in MSO principal cell somata (Scott et al., 2010). The high-threshold potassium channel was modeled according to Rothman and Manis (2003) without a slow activation variable and only at the soma since it had only little effect in the axon. The low-threshold potassium channel (KLT) was modeled according to (Mathews et al., 2010) and was present in the soma and all unmyelinated axonal compartments. The potassium reversal potential was set to −90 mV. The hyperpolarization-activated cation channel gives rise to a somatic hyperpolarization (h)-activated cation current (I_h), which was modeled using the kinetics measured in dorsal MSO neurons (Baumann et al., 2013), with a reversal potential of −35 mV. The resting potential of −68 mV and the somatic input resistance of 5 MΩ were set by adjusting the peak conductances of KLT and h current. The somatic surface was set to 8750 μm^2, such that we get a somatodendritic capacitance of 70 pF (Rautenberg et al., 2009), assuming a specific capacitance of 0.8 $\mu F/cm^2$ (Gentet et al., 2000; Shu et al., 2007). As a consequence, the somatic membrane time constant is 350 μs, which closely resembles the measured membrane time constants *in vitro* (Scott et al., 2005; Couchman et al., 2010). The specific myelin conductance per lamella was set to 0.1 $\mu F/cm^2$ (McIntyre et al., 2002, 2004). Together with a g-ratio of 0.7 and an assumed myelin periodicity of 16 nm (Agrawal et al., 2009), our standard model exhibits nine myelin lamellae. Thus, we obtain a specific capacitance of the myelin sheath of 0.0111 $\mu F/cm^2$, similar to the value of 0.01 $\mu F/cm^2$ used in Kuba et al. (2006) for axons of nucleus laminaris (NL) neurons. Some computational studies of axons use specific capacitances per lamella that are significantly higher; however, they compensate for this by a larger number of myelin lamellae. Using a substantially larger myelin capacitance (e.g., three times or higher) would cause propagation failures of generated APs in our model, a result that would contradict the secure propagation of APs known from MSO principal neurons (Scott et al., 2007). This matching of an experimental finding argues in favor of our parameter choice. The validity of the parameter choice is further supported by our physiological measurements of firing thresholds for onset-like responses in Figure 4.

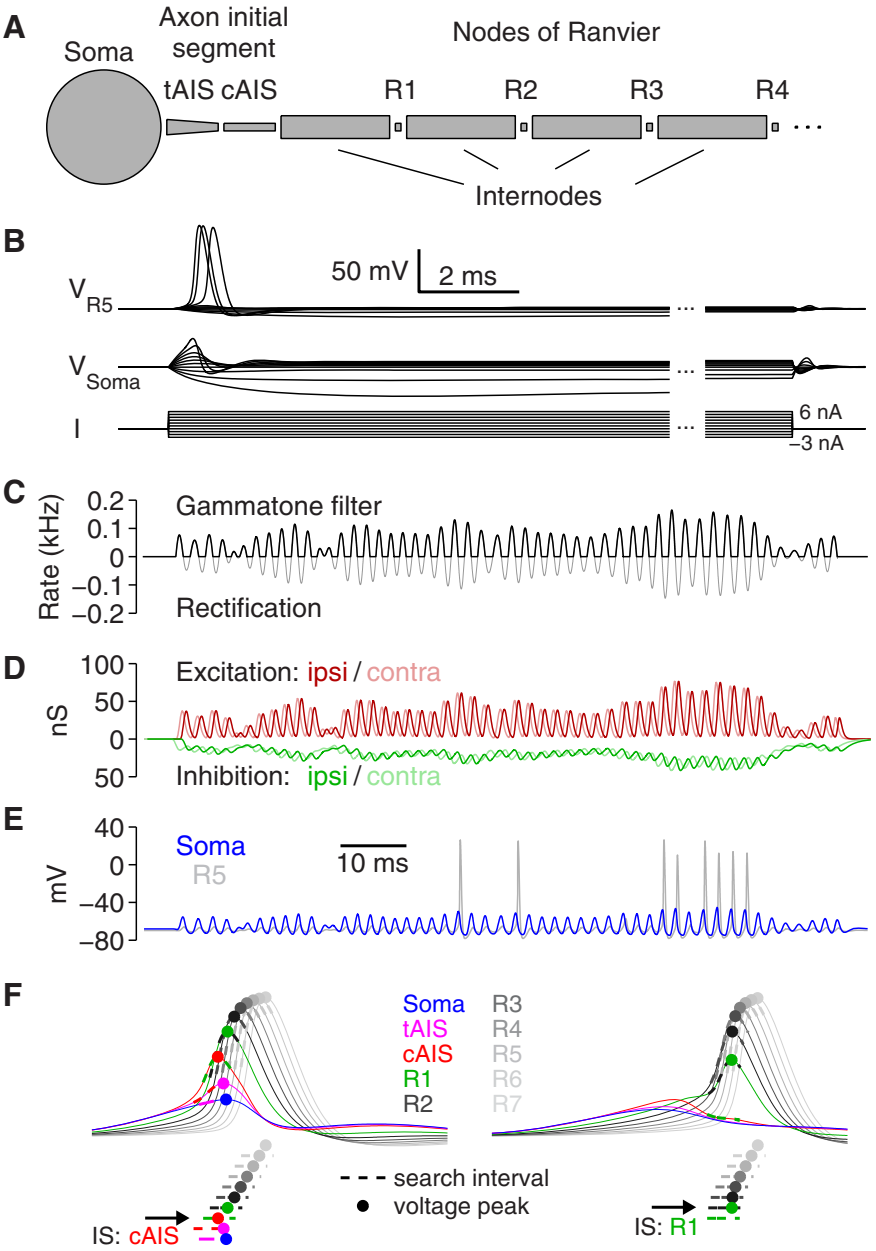

Figure 1. Computational model. ***A***, Schematic drawing of the first segments from the soma to R4 of the MSO model neuron. The AIS is subdivided into two compartments: the tAIS and the cAIS. ***B***, Voltage response in different compartments (top, R5; middle, soma) to current injections at the soma (bottom). ***C***, ***D***, The input conductances were obtained from noise that is filtered by a gammatone filter with a center frequency of 500 Hz (gray) and half-wave rectified (***C***, black). The trace from ***C*** is transformed into conductance inputs by convolution with excitatory (ipsilateral, dark red; contralateral, light red) and inhibitory (ipsilateral, green; contralateral, light green) synaptic kernels (***D***; see Materials and Methods). ***E***, Voltage responses of the soma (blue) and R5 (light gray) of the model when driven with the conductance trains depicted in ***D***. ***F***, The AP initiating segment (IS, black arrow) is derived from the voltage traces at the individual compartments (color coded segments: blue, soma; pink, tAIS; red, cAIS; green, R1; dark gray to light gray, R2–R7). Example traces show a cAIS-generated (left) and an R1-generated (right) AP. Dashed traces indicate the search intervals of duration *L* that are defined by the voltage peak (dot) of the downstream segment (see Materials and Methods). The voltage peak that occurs earliest in time defines the SIS.

A detailed account of the geometrical and electrical features of the model is given in Tables 1 and 2, respectively.

In response to somatic current injections, the neuron model exhibits typical onset behavior (Fig. 1*B*; i.e., it fires only one AP; Scott et al., 2005; Couchman et al., 2010) at the onset of the depolarizing pulse. The AP amplitude at the soma resembles physiologically measured values of ~10 mV (Scott et al., 2005; Couchman et al., 2010), whereas, at the nodes of Ranvier, the APs exhibit usual amplitude values of ~100 mV.

Table 1. Geometrical parameters of the model

Parameters	Values
Soma/somatodendritic compartment	
Area	8750 μm^2
Axon initial segment (tapering part)	
Length	10 μm
Large diameter	1.64 μm
Small diameter	0.66 μm
Axon initial segment (constant part)	
Length	10 μm
Diameter	0.66 μm
Internodes	
Length	100 μm
Inner diameter	0.66 μm
Outer diameter	0.948 μm (corresponding to a g-ratio of 0.7),
Myelin lamellae	9 (corresponding to a myelin periodicity of 16 nm)*
Node(s) of ranvier	
Length	1 μm
Diameter	0.66 μm

*From Agrawal et al. (2009).

Table 2. Maximum conductances of voltage-gated channels

Channels	Soma	tAIS	cAIS	Internodes	Nodes
gNa	0.2	4	4	0	4
gKHT	0.1	0	0	0	0
gKLT	1.55	1.55	1.55	0	1.55
gh	0.02	0.02	0.02	0	0
glk	0.0005	0.0005	0.0005	0.0002	0.05

Data are in nS/μm^2.

Since ongoing synaptic bombardment under *in vivo* conditions increases the leakiness of the neuron, we decided to study AP generation using a temporally extended naturalistic stimulus that resembles the periodicity of a cochlear channel with a specific center frequency. Our stimuli were generated using bandpass-filtered white noise $n(t)$ (Fig. 1*C*) that was linearly filtered (convolved) with a gammatone kernel, as follows:

$$f(t) = t^4 e^{-t\gamma} \cos(t\omega_c),$$

with $\gamma(\omega_c) = 24.7(4.37 \times \omega_c/(2\pi)+1)$ in kilohertz (Glasberg and Moore, 1990) and the center frequency $\omega_c/(2\pi)$ in kilohertz. The filter output was half-wave rectified and normalized to yield a spike probability function with a mean AP rate R (200 Hz) during the stimulus length l = 300 ms. The resulting input train was then multiplied with a factor S, which we call the stimulus intensity, and afterward convolved with double-exponential functions G_{exc} and G_{inh}, which we created to resemble electrophysiologically measured synaptic kinetics for excitatory and inhibitory synaptic activity (Couchman et al., 2010):

$$G_{exc}(t) = g_{exc} \frac{(1 - e^{-t/1.0})^{1.3}\, e^{-t/0.27}}{\max((1 - e^{-t/1.0})^{1.3}\, e^{-t/0.27})} \text{ and}$$

$$G_{inh}(t) = g_{inh} \frac{(1 - e^{-t/0.4})\, e^{-t/1.6}}{\max((1 - e^{-t/0.4})\, e^{-t/1.6})}.$$

Here, g_{exc} = 37 nS and g_{inh} = 57 nS are the peak conductances of single fibers (Couchman et al., 2010), and time t is considered in milliseconds. Examples for such synaptic conductance trains are shown in Figure 1*D*. Unless mentioned otherwise, we used two inhibitory inputs based on the same stimulus wave form; one advances the excitatory inputs by 0.6 ms and one lags them by 0.11 ms (see Impact of distal AP initiation on ITD coding; Leibold, 2010). Apart from the simulations in which the inhibitory inputs are essential (see Figs. 5*M*, 8), all simulations were performed with only excitatory inputs activated.

Neuron model with dendrites

To test the robustness of our findings in a model with dendrites, we performed simulations (see Fig. 8) in a model variant in which two identical dendrites (five compartments each) were added to the soma. Excitatory synapses were placed at the dendrites (ipsilateral inputs at the lateral dendrite, contralateral inputs at the medial dendrite), and inhibitory synapses were restricted to the soma (Kapfer et al., 2002). The parameters of the dendritic model were chosen such that the basic characteristics at the soma (input resistance, resting potential, capacitance, and EPSP kinetics) matched that of the model with a single somatodendritic compartment and hence the physiological data from Scott et al. (2005) and Couchman et al. (2010). Most importantly, the length of each of the dendrites was 200 μm, with a constant diameter of 5 μm. The somatic surface was reduced to 2467 μm^2, such that the total cell surface remained at 8750 μm^2, which is equal to the model with only one somatodendritic compartment. The geometrical length of the dendritic compartments appears slightly longer than that observed in MSO neurons (Rautenberg et al., 2009), since we did not take into account branching of dendrites but had to match the overall cell surface for comparability.

In the dendritic compartments, sodium channels were omitted (Scott et al., 2010), and thus the sodium density of the remaining somatic compartment was scaled up such that the total sodium conductance matched that of the simpler model with only one somatodendritic compartment. The conductance of the low-threshold potassium channels decayed exponentially along the dendrites with a length constant of 74 μm (Mathews et al., 2010). The peak conductance at the somatic compartment was thereby identical to that of the simpler model. The conductance of the h current was chosen to follow the same gradient along the dendrite to keep the local balance of the two channels. Finally, the input resistance and resting potential of the model with dendrites were matched to those of the simpler model by adjusting the peak conductances of the h current and the passive leak current.

Analysis of simulations

In our simulations, APs during ongoing stimulation were often not detectable in the soma (Fig. 1*E*). However, at more distal locations in the axon, the amplitude and kinetic differences of subthreshold responses and APs are much larger, and, thus, at the more distal axonal compartments these two cases are very easy to separate by a simple amplitude threshold.

Initiating segment. Since the MSO model is described by a system of coupled differential equations, the generation of an AP necessarily requires the interplay of all compartments. The question of where an AP is generated thus can only be answered by a phenomenological criterion. This phenomenological AP-initiating segment was identified as follows (Fig. 1*F*). First, a stimulus evoked AP was defined by a voltage threshold criterion in R7 at which AP and no AP events are clearly separable. Second, we inspected the voltage trace at the axonal nodes of Ranvier and the AIS going from distal to proximal, and identified the segment-specific AP times via the voltage peaks (above −50 mV) that occurred within a certain time interval of duration L around the voltage peak in the (previous) downstream node. The duration L of this time interval is determined by $L = 5.33\ \lambda$, where λ is the impulse conduction time from node to node for a strong current stimulus delivered at rest, which elicits a clear AIS AP. The window is asymmetrically aligned to the previous voltage peak such that the preceding part is three times longer than the part following the voltage peak. The factor 5.33 allows for a slower AP propagation of the AIS and near-threshold stimuli. Within the set of all detected voltage peaks, the earliest in time defines the AP initiation segment. This algorithm has been tested against a variety of simple threshold and phase space criteria, and has proven to give more reliable results for different axonal morphologies and different input parameters, even for extremely fast voltage deflections.

In simulations in which we tested higher somatic input resistances (see Fig. 5*L*), the somatic AP was strongly influencing the voltage trace in the AIS, which made it difficult to identify a clear AIS voltage peak. We therefore identified the AIS AP as the first drop of the voltage derivative below 50 V/s, identifying a shoulder in the voltage deflection.

In few cases (see Fig. 6) during orthodromic propagation does the AP amplitude initially decrease before increasing again in the more distal

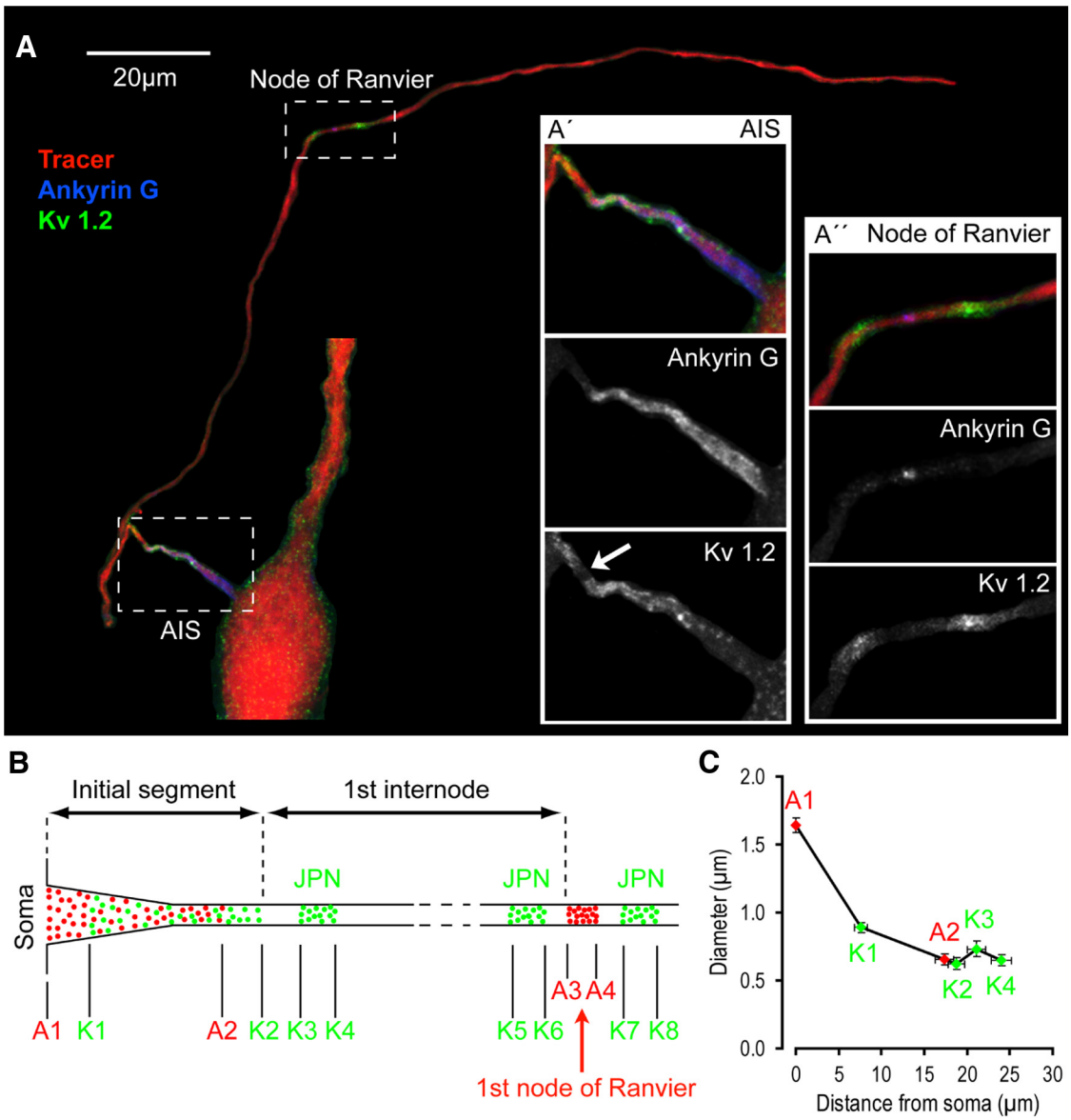

Figure 2. Morphometry of the AIS and first internodal segments in MSO neurons. ***A***, Retrogradely labeled MSO neuron after digital extraction from the surrounding area. Insets ***A′*** and ***A″*** show magnifications of the AIS and first node of Ranvier, respectively. ***B***, Schematic of the proximal axon segment comprising the AIS, the first internode, and the first node of Ranvier, illustrating the positions where measurements were made. Red and green dots indicate the distribution of ankyrin G and Kv1.2 immunolabeling in the AIS and axon. A1–A4 and K1–K8 indicate the borders of ankyrin G- and Kv1.2-positive domains, respectively. JPN, Juxtaparanodes. ***C***, Mean diameter of the AIS at various positions plotted as a function of the mean distance from the soma. Diameter and distance measurements were made at the positions indicated in ***B***. Error bars show the SEM.

axonal segments. Such APs were also labeled as being distally initiated, even though they would have been an AIS AP according to the time-window criterion.

Relative slope during ongoing conductance trains. To identify the input features that are most predictive for spiking, we placed particular emphasis on current amplitude and the relative current slope (derivative divided by amplitude). We chose relative slope because the derivative of any oscillating function linearly scales with the amplitude of the input, and, thus, without such normalization, dependencies on slopes are confounded by amplitude effects. To determine the relative derivative of the input current in Figure 7, *G* and *H*, we normalized by the amplitude of a high-pass-filtered version (fourth-order Butterworth filter with a cutoff of one-third of the stimulation frequency) of the input current rather than by the actual amplitude itself. This was necessary to obtain the actual local relative slope for each cycle and not a distorted value caused by the temporal summation of the input currents of high-frequency stimuli.

ITD coding

To assess how well the responses of the model neuron resolve an ITD τ, we computed the Fisher information $I(\tau)$, assuming a Gaussian distribution of AP counts. From at least 90 repetitions of a 300 ms stimulus, we obtained the mean AP count (tuning curve) $\mu(\tau)$ and its variance $\nu(\tau)$, and calculated the Fisher information as follows:

$$I(\tau) = \frac{\mu'(\tau)^2}{\nu(\tau)} + \frac{1}{2}\left(\frac{\nu'(\tau)}{\nu(\tau)}\right)^2$$

Results

Morphometry of the AIS and proximal axon

Using a combination of retrograde tracing of MSO neurons and immunohistochemical labeling of ankyrin G and Kv1.2 channels, a detailed morphometric analysis of the AIS and proximal axon of

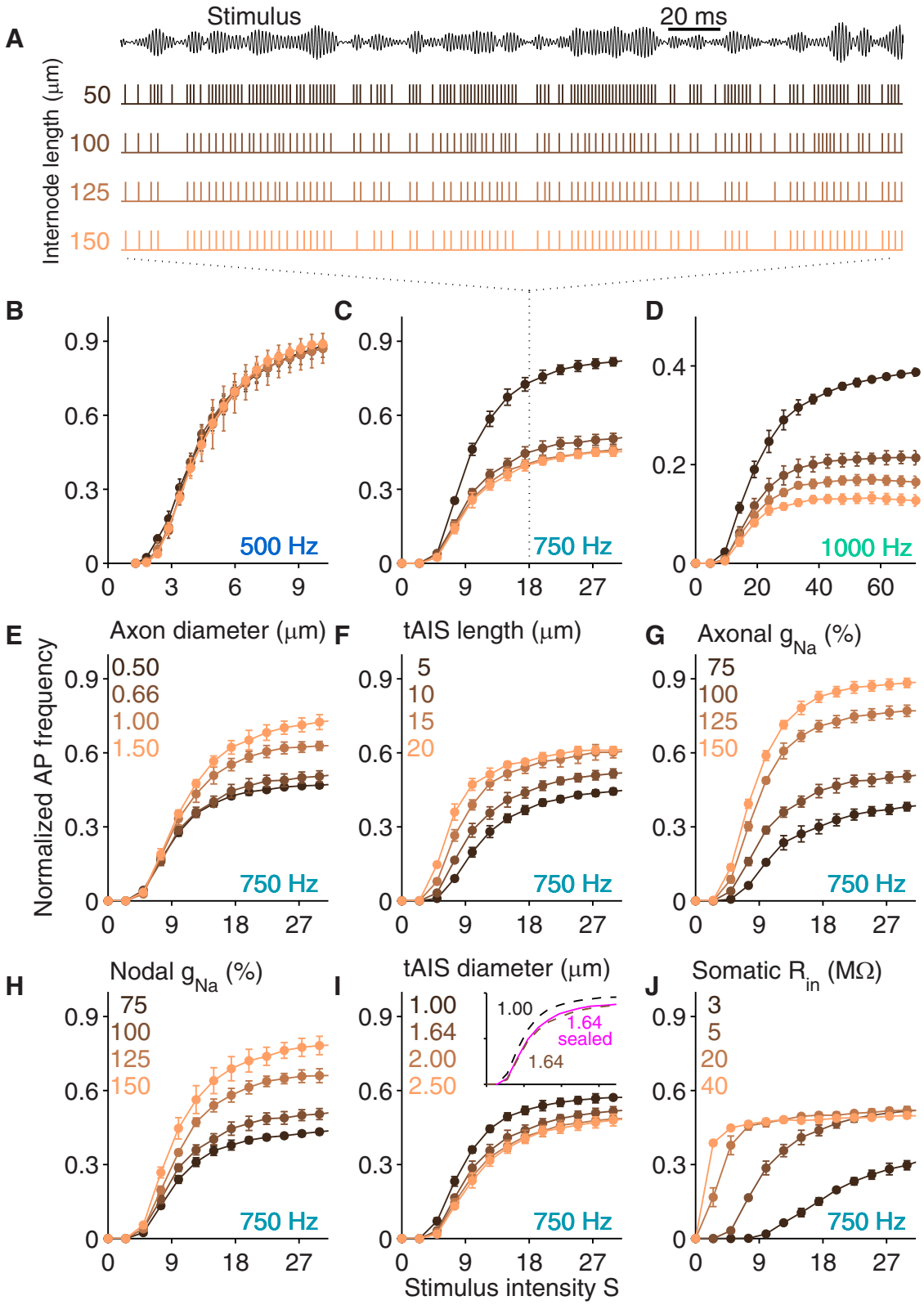

Figure 3. Input/output functions of the model. ***A***, Spike trains were simulated for bandpass stimuli (top trace) of duration 300 ms. The four spike trains are derived from the same (frozen noise) stimulus with a center frequency of 750 Hz and intensity $S = 18$ (as indicated by dotted lines) and internode lengths as indicated by colors. ***B–J***, Graphs depict firing probabilities for different (color-coded) morphological parameters and sodium conductances and for increasing stimulus intensities S (see Materials and Methods). Parameters that were varied are internode length (color coded) and center frequency (***B–D***), axonal diameter (***E***), length of the AIS tapering part (***F***), peak sodium conductance in all unmyelinated parts of the axon (***G***), peak sodium conductance in the nodes of Ranvier (***H***), proximal diameter of the AIS tapering part (***I***), and somatic input resistance (***J***). Inset in ***I*** compares relative AP frequencies of two control traces (with different tAIS diameter) from ***I*** to a model where all subthreshold transmembrane conductances were removed from the tAIS (pink trace, sealed).

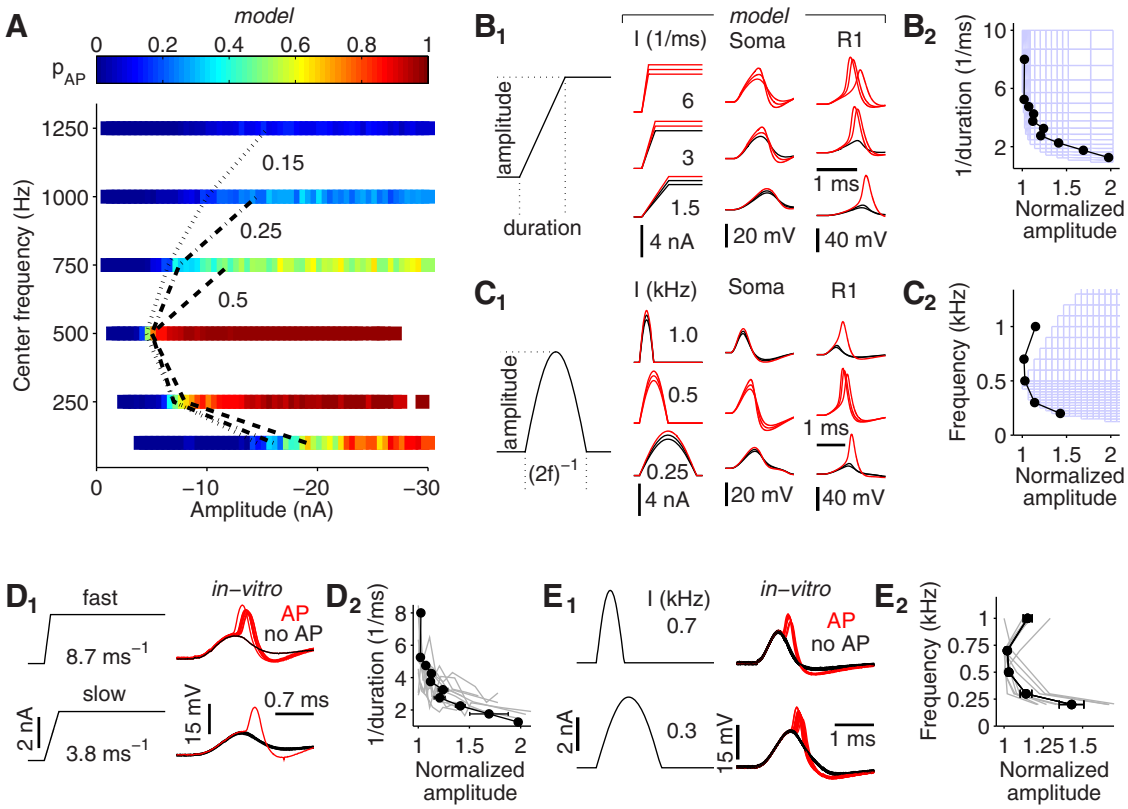

Figure 4. Frequency-dependent AP threshold. ***A***, Firing probability (color coded) of the model cell as a function of center frequency and cycle amplitude for ongoing inputs. Iso-probability contours are shown for firing probabilities of 15% (dotted trace), 25% (dot-dashed trace), and 50% (dashed trace). ***B₁***, Ramp stimulus (left) and raw data of the simulation for three different ramp durations (right). Black and red traces indicate subthreshold and AP responses, respectively. ***B₂***, Light blue mesh shows parameter region that evoked an AP response. *In vitro* threshold is overlaid as a black line (see ***D***). ***C***, same as ***B***, for half-wave-rectified sine stimuli. ***D***, ***E***, *In vitro* results. ***D₁***, Stimuli (left) and current-clamp traces (right) for the ramp stimulus experiment. ***D₂***, Threshold curves from individual neurons (gray traces) and their average (black, $n = 12$, same as in ***B₂***). ***E***, same as ***D***, but for half-wave-rectified sine stimuli *in vitro* ($n = 8$). The data of ***B***–***E*** were normalized to the smallest amplitude that elicited an AP response in the specific cell. Error bars show the SEM.

12 MSO neurons was performed (Fig. 2*A*). Our immunostainings revealed that the AIS consisted of a 17.3 ± 1.1-μm-long ankyrin G-positive domain emerging directly from the soma and a 11.2 ± 0.6-μm-long Kv1.2-positive domain starting at 7.6 ± 0.7 μm distal from the soma in the labeled axons (Fig. 2*A*,*B*). Diameter measurements indicated that the AIS consisted of the tAIS and the cAIS. On average, the diameter of the AIS decreased from 1.6 ± 0.1 μm at the soma (position A1) to 0.6 ± 0.1 μm at the position K2, as defined in Figure 2, *B* and *C*. The length of the AIS (measured from A1 to K2; Fig. 2*B*) ranged from 14.0 to 24.0 μm (18.8 ± 1.0 μm). Adjacent to the AIS was a 2.3 ± 0.2-μm-long segment devoid of ankyrin G and Kv1.2 labeling, which we interpret as the paranodal (or para-AIS) region, where myelin is anchored to the axon (Duflocq et al., 2011; Fig. 2*A*′, arrow). The paranodal region was followed by a 2.9 ± 0.5-μm-long Kv1.2-positive domain representing the juxtaparanode (or juxtapara-AIS). The first node of Ranvier was identified based on its typical arrangement of two juxtaparanodal Kv1.2-positive domains that were separated from the nodal ankyrin G domain through unlabeled paranodes (Fig. 2*A*′). The length of the first internode ranged from ~50 to ~150 μm (100.4 ± 9.1 μm), and its mean diameter (Fig. 2*B*,*C*, measured at several positions between the two juxtaparanodal borders K3 and K6) was 0.7 ± 0.1 μm. These axonal parameters were used to constrain a computational model of the MSO neuron (Table 1).

Input–output functions

We first determined how the AP frequency of our computational neuron model is influenced by the parameters that we assumed to be most crucial for axonal excitability (AP threshold), i.e., the morphological parameters internode length, axonal diameter, proximal diameter, and tAIS length; and the electrical properties density of sodium channels in the unmyelinated axonal segments and somatic input resistance (Fig. 3). We tested how much the influence of these excitability parameters on AP probability depended on the center frequency of the bandpass stimuli (see Materials and Methods) and found that for center frequencies of ≤500 Hz all of the axonal parameters had little influence on spiking probability (Fig. 3*A*–*D*, example of internode length). For higher stimulus frequencies, the axonal parameters had distinct influences on the input–output functions. As we increased the internode length, the spiking probability generally decreased (Fig. 3*A*–*D*), which can be attributed to a reduction of the axial current flow. Geometrical alterations that increase the axonal sodium conductance (while keeping the channel density constant) mostly result in an increase of the firing rate. This increase could be observed in simulations with altered axonal diameter [keeping a constant ratio of 0.7 between the inner (axon) and outer (myelin) diameter of the internode]. The firing rate also increased with axonal diameter (Fig. 3*E*), reflecting the corresponding increase of the number of sodium channels. Also an increase of the length of the tAIS led to a higher AIS sodium

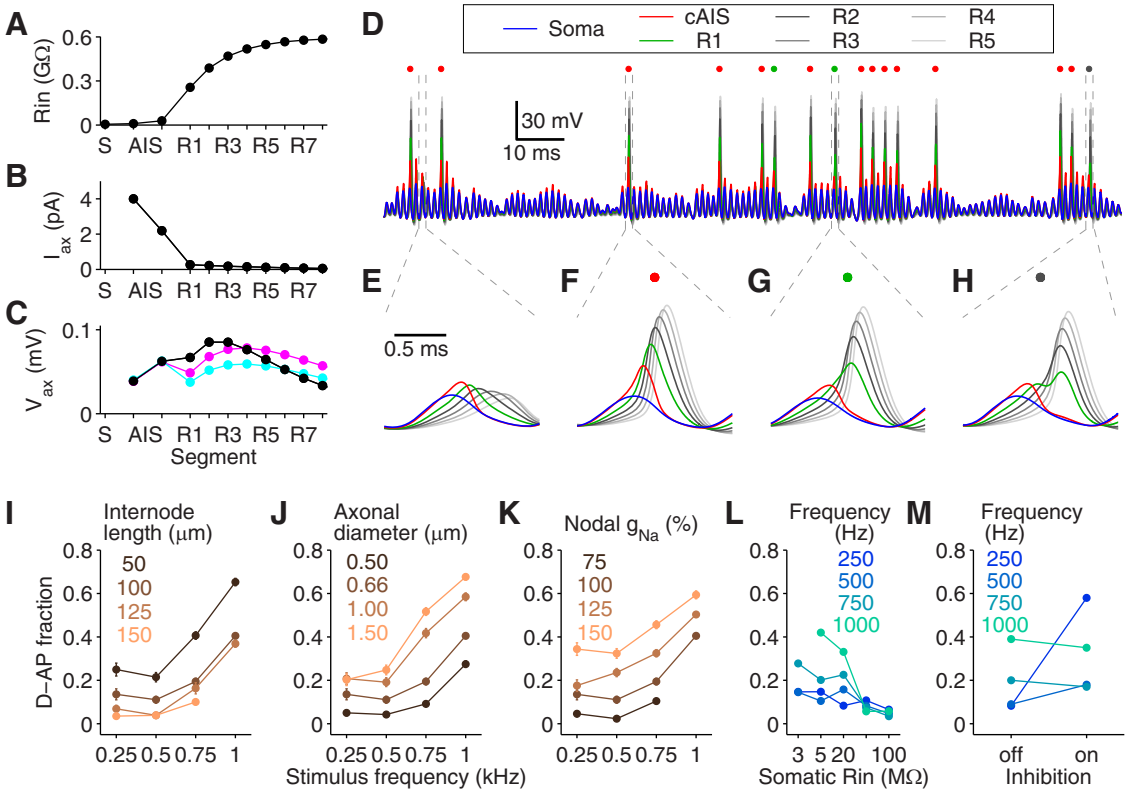

Figure 5. Distal AP initiation. ***A–C***, Local input resistance (***A***), axial current (***B***), and V_{ax} (***C***) in the different model compartments for the standard parameters (black traces), the model with shorter internode lengths of 50 μm (magenta traces), and thicker axonal diameter of 1.5 μm (cyan traces). ***D***, Exemplary voltage traces in different compartments (colors as indicated). Filled colored circles show the AP-initiating segment for each suprathreshold response (see legend). ***E–H***, Example events (from ***D***) for subthreshold response (***E***), and evoked APs generated in the AIS (***F***), R1 (***G***), and R2 (***H***). ***I–K***, Fraction of distally initiated APs (D-AP; for a fixed AP probability of 15%), with varying internode length (***I***), axonal diameter (***J***), and sodium conductance in the nodes of Ranvier (***K***). ***L***, Fraction of distally initiated APs for different somatic input resistances. ***M***, Fraction of distally initiated APs without and with inhibition for several input frequencies.

conductance and an increasing firing probability (Fig. 3*F*). In line with these findings, a direct increase in the sodium conductance in unmyelinated axonal compartments (Fig. 3*G*,*H*) also facilitated AP probabilities. However, a different effect was observed when the proximal diameter of the tAIS was decreased, which also decreased the amount of sodium conductance but, interestingly, increased AP frequency (Fig. 3*I*). This indicates that in addition to the total local sodium conductance excitability of the axon also profits from an increased electrotonic isolation from the leak currents in the soma. This interpretation was corroborated by the following two additional sets of simulations: (1) an increase of the tAIS input resistance by removing all tAIS subthreshold conductances from the equation had almost no effect on firing probability (Fig. 3*I*, inset); and (2) increasing the somatic input resistance (by multiplicative scaling of the peak conductances of KLT channel and h current, keeping a constant resting potential) strongly enhanced AP frequency (Fig. 3*J*). The MSO soma thus acts as a strong current sink for the AIS, and, hence, the axon excitability crucially depends on rather small changes of the somatic current reaching the axon.

Frequency-dependent threshold

Since the firing probabilities strongly depended on the center frequency of the inputs (Fig. 3), we performed a more systematic analysis of the frequency dependence of excitability of our computational neuron model and corroborated these data by *in vitro* measurements of MSO cells. The frequency dependence of MSO firing probability in the model was determined for a large range of bandpass stimuli with center frequencies ranging from 100 to 1250 Hz and varying stimulation intensities (Fig. 4*A*). This allows the assessment of the firing thresholds of MSO neurons with respect to both the shape (frequency content) and the amplitude of the input currents. The lowest current thresholds were observed at ~500 Hz. For higher as well as lower input frequencies, more excitatory drive was necessary to reach a certain firing probability.

To better understand the dependence of AP initiation on the input kinetics, we simulated two onset stimulation paradigms using brief current stimuli applied at rest. First, we applied a ramp stimulus for which we could independently vary amplitude and ramp duration (Fig. 4B_1). The ramp duration was assumed to serve as a proxy for stimulus shape (frequency) during the ongoing bandpass stimulation. The firing probabilities (Fig. 4B_2) obtained with these stimuli very well explained the behavior observed for low-frequency bandpass inputs, which effectively implements a slope threshold (Golding and Oertel, 2012); that is, the neuron fires in response to a specific speed of membrane depolarization that is rather independent of amplitude. Such behavior has been previously described in octopus cells (Ferragamo and Oertel, 2002), in the vestibular pathway (Beraneck et al., 2007) and the MSO (Jercog et al., 2010), and is generally attributed to the fast kinetics of the KLT channels, which are further opening only for slow stimuli and cannot generate such additional leaks for fast-rising stimuli. The high-frequency behavior of our threshold profile, however, could not be modeled using the simple ramp stimuli. We therefore also applied half-wave-rectified sine waves (Fig. 4C_1). Here again, both the low- and the high-frequency increase of threshold amplitudes was observed

(Fig. 4C_2). Thus, the threshold amplitude for high frequencies crucially depends on the duration of the stimulus. This indicated that the high-frequency part of the threshold curve reflects the limit imposed by the charging of the membrane capacitor for regimes in which the membrane voltage rises too quickly to open the low-threshold potassium channels (Jercog et al., 2010). These modeling results were verified physiologically using whole-cell current-clamp recordings using the same stimuli as in the model (see Materials and Methods). From the recorded data obtained with the ramp stimuli, the AP probability was fitted by a sigmoid for each ramp duration as a function of the amplitude using at least 10 consecutive trials. The amplitude at which the fit was at 50% AP probability was defined as the threshold. The physiologically obtained threshold curves qualitatively matched the modeling results for the ramp-current stimuli (Fig. 4B_2, superimposed black trace, *D*) with less firing for slow-input ramps and secure responses for faster ramps. For the half-wave-rectified sine stimuli, threshold amplitudes were obtained by manual testing (Fig. 4C_2, superimposed black trace, *E*) and also qualitatively matched the simulations with the lowest firing threshold for medium frequencies and less firing for low and high frequencies. From these simulations and experiments, we concluded that the threshold behavior observed during ongoing stimulation is functionally very similar to that in onset-like stimulus paradigms with single current pulses.

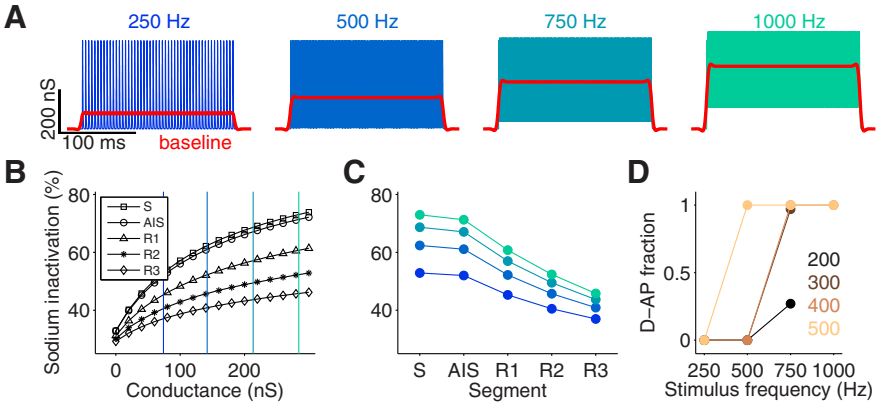

Figure 6. High input frequencies cause sodium channel inactivation in the somatic and proximal axonal membranes. ***A***, Periodic synaptic conductances with a peak value of 400 nS for center frequencies of 250, 500, 750, and 1000 Hz. Red traces are obtained by low-pass filtering the voltage traces (cutoff frequency, 100 Hz). ***B***, Steady-state sodium channel inactivation measured in different model compartments for increasing excitatory conductances. ***C***, Steady-state sodium channel inactivation for traces (color coded) in ***A*** in different compartments. ***D***, Fraction of distally initiated APs (D-APs) for input traces in ***A*** with different conductance peak values (color coded; in nS).

Site of AP initiation

Although AP initiation might be functionally similar under onset and ongoing stimulus conditions, the underlying mechanisms may be different, since, owing to the temporal summation of the inputs, the ongoing stimulation sets the cell membrane into a state that is very different from resting conditions (e.g., because of steady-state activation of channels and changes in input resistance). We therefore investigated AP initiation during ongoing stimulation in greater detail. In particular, we were interested in the contributions of the different cellular (somatic and axonal) compartments to the generation of APs.

A first assessment of the local excitability of the model neuron was derived from local input resistance measurements, using small hyperpolarizing current pulses (amplitude, −100 pA for 300 ms) that were consecutively injected into the soma, the cAIS, and the nodes of Ranvier of our model at rest (Fig. 5*A*, black trace). Here, the input resistance was derived from the peak of the voltage responses and not the steady-state component to obtain a measure for the instantaneous susceptibility of the local membrane. In our model, the peak conductance parameters were chosen such that the somatic input resistance was fixed at 5 MΩ (Scott et al., 2005; Couchman et al., 2010). With the standard parameter settings (Tables 1 and 2), the AIS had two (tAIS, 9.7 MΩ) to six times (cAIS, 28.5 MΩ) the input resistance of the soma. Further distally in the axon, the R1 showed a 50-fold increase of input resistance (256.5 MΩ). We next applied a current pulse of 1 nA at the soma while at the same time extracting the peak of the axial current in the respective axonal segments (Fig. 5*B*, black trace). The portion of this current that spread from the soma into the AIS was only 0.4% (4 pA), with further attenuation at the R1 (0.3 pA). Multiplying the axial current by the local input resistance yields a measure that can be interpreted as the axonally mediated voltage amplitude (V_{ax}). This voltage amplitude was further used as an estimate for the local excitability. The axially mediated voltage amplitude was maximal at the second and third nodes of Ranvier (Fig. 5*C*, black trace). Thus, in contrast to the classical model of AP initiation at the AIS, the second and third nodes appear to be more excitable, indicating that the more distal compartments play an important role in axon excitability in leaky neurons.

A detailed analysis of AP times in the individual compartments revealed that the site of AP initiation was indeed not restricted to the AIS (Fig. 5*D–H*). Although many APs were initiated in the AIS (Fig. 5*F*,*I–K*), 5–60% (depending on input conditions) of the APs first crossed the detection threshold (see Materials and Methods) at the first (Fig. 5*G*) or even the second (Fig. 5*H*) node of Ranvier, while the AIS showed a response similar to the subthreshold case (Fig. 5*E*). The amplitudes of the somatic and AIS APs were relatively small, independent of where they were generated, and underwent subsequent amplification by the nodes of Ranvier as they orthodromically propagated along the axon (Fig. 5*F–H*).

To further elucidate the mechanisms of this distal AP initiation, we quantified its occurrence under our naturalistic ongoing input paradigm for different morphological parameters. For purely excitatory inputs, the fraction of distally initiated APs over AIS APs increased with stimulus frequency (Fig. 5*I–L*). For shorter internodes (Fig. 5*I*) and thicker axonal diameter (Fig. 5*J*), more distal APs were observed. This is because the resulting increased axial conductance allows the stimulus-evoked potential to propagate further along the axon and is also illustrated by the peak of the V_{ax} located at more distal regions of the axon in both conditions (Fig. 5*C*, cyan and magenta traces). Consistently, a higher nodal sodium conductance increased the fraction of distally initiated APs as well, because APs could be more easily initiated at the nodes (Fig. 5*K*).

A major factor influencing distal AP initiation for inputs at all center frequencies is the somatic input resistance. The prevalence of distal AP initiation is strongly reduced with the increase of input resistance of the soma (Fig. 5*L*). Hence, distal spiking

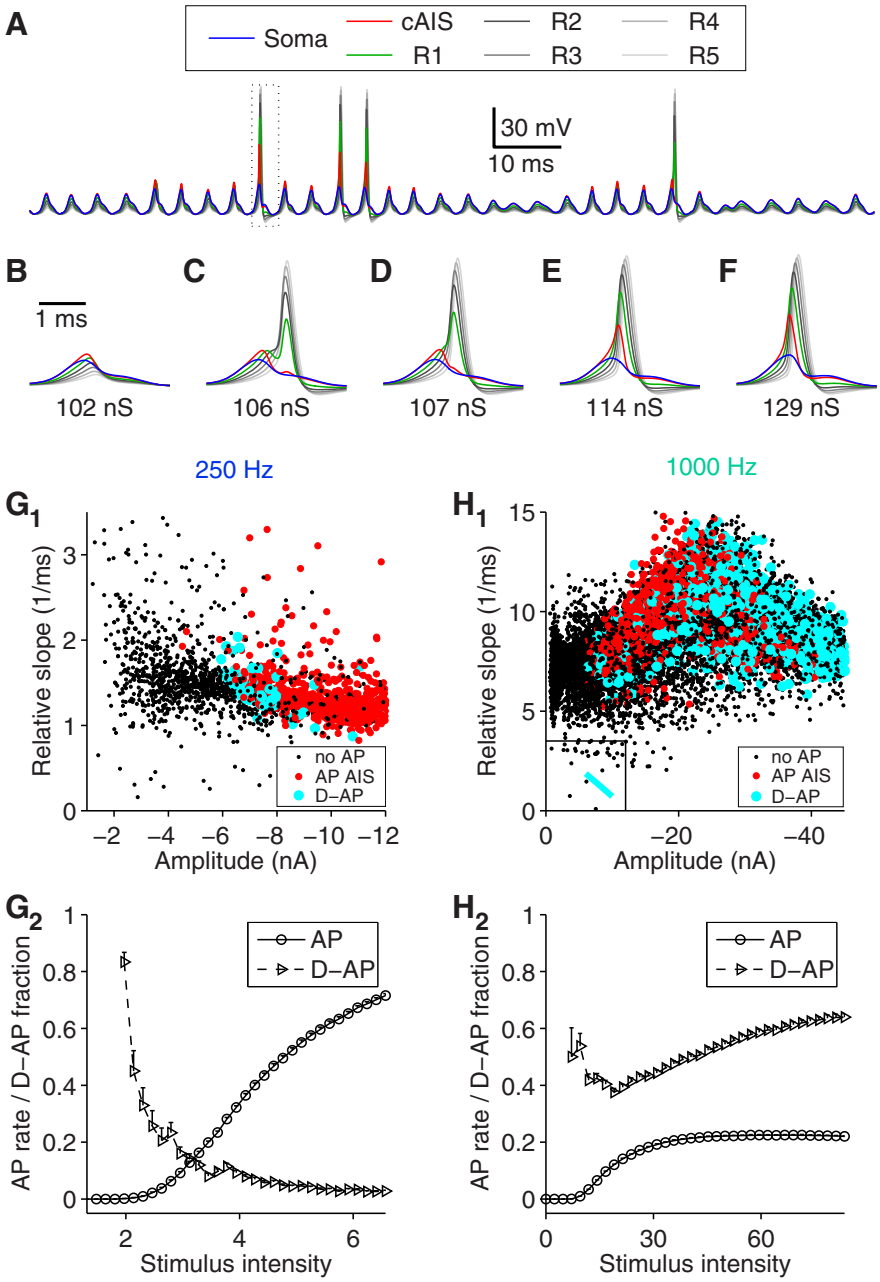

Figure 7. Function of distal AP initiation. ***A***, Example voltage traces for a stimulus with center frequency 250 Hz. The box indicates a cycle that was further investigated for different excitatory peak conductance values. ***B–F***, The selected stimulus cycle evolves from a subthreshold response (***B***), via a distally initiated AP (***C***, ***D***), to an AP initiated in the AIS (***E***, ***F***). G_1, Model responses to input trains with a center frequency of 250 Hz generate a broad range of cycle amplitudes and relative derivatives (see Materials and Methods). Each dot corresponds to a cycle within the input train. Black, Subthreshold response; red, AP response initiated in the AIS; cyan, AP response initiated in a node of Ranvier (D-AP). G_2, Firing rate and fraction of distally initiated APs for increasing excitatory synaptic conductances and an input with 250 Hz center frequency. H_1, Same as G_1 for an input with a center frequency of 1000 Hz. The cyan line in the box is a linear fit to the distally initiated APs from G_1. H_2, Same as G_2 but for inputs with 1000 Hz center frequency.

should be particularly prevalent in leaky neurons that receive fast-fluctuating inputs such as in the MSO.

Since MSO neurons not only receive excitatory inputs but also strong phase-locked inhibitory inputs via the medial and lateral trapezoid body, we also performed simulations with excitatory and inhibitory inputs. In these simulations, the frequency dependence of the site of AP initiation is less clear (Fig. 5*M*). On the one hand, the fraction of distally initiated APs also increased with frequency for center frequencies of >500 Hz. On the other hand, for a low center frequency of 250 Hz, inhibition also generated large amounts of distal AP initiation. This already indicates that distal AP initiation may result from a variety of different mechanisms, particularly also those that add to the somatic current sink.

Distal AP initiation for high-frequency inputs

The steady-state approach to axonal excitability (Fig. 5*A–C*) disregards contributions from the dynamics of the ion channels. To understand whether such dynamic properties of the neuron model also contribute to distal AP initiation, we used strictly periodic synaptic (conductance) input trains of different frequencies (Fig. 6*A*). Temporal summation of the synaptic inputs generated a conductance plateau that increased with frequency as revealed by low-pass filtering (Fig. 6*A*, second-order Butterworth low-pass filter with a cutoff frequency of 100 Hz, red traces). We then applied these average conductance values as a constant conductance to the cell and measured the corresponding steady-state sodium channel inactivation at the soma, the AIS, and the first three nodes of Ranvier (Fig. 6*B*). This revealed that a larger average conductance generally caused more sodium channel inactivation. Moreover, the conductance level was highest at the soma and decreases along the axon. Thus, a regime of a high-frequency input generates a persistent depolarization of the membrane with a larger fraction of inactivated sodium channels at the proximal axonal membranes than at the distal segments (Fig. 6*C*). As a result, this leads to a larger fraction of distal AP initiation with increased input frequency (Fig. 6*D*).

Influence of distal AP initiation on the firing threshold

To understand the functional relevance of distal AP initiation, we next investigated which input properties are particularly amenable to evoke distal APs during ongoing stimulation (Fig. 2*B–D*). We therefore repeatedly stimulated the neuron model with identical input trains for consecutively increasing mean synaptic conductances. Figure 7*A–F* shows an exemplary stimulus cycle for which, with increasing conductance, the voltage profile along the axon transitions from a completely subthreshold response (Fig. 7*B*) over an AP being initiated at the nodes of Ranvier (Fig. 7*C*,*D*) to an AP generated at the AIS (Fig. 7*E*,*F*). From these examples, it seemed that distal AP initiation is particularly prevalent at the AP threshold.

To further evaluate the threshold property of distal AP initiation, we ran the simulations using excitatory bandpass inputs of

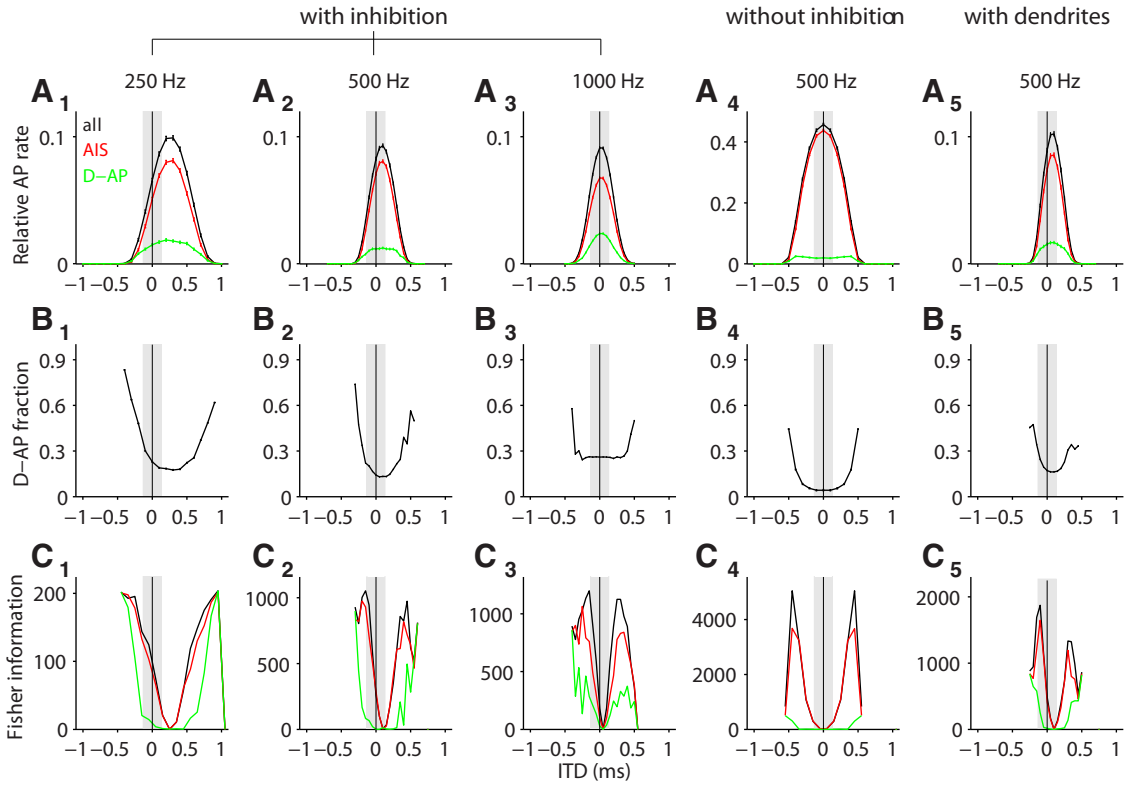

Figure 8. Representation of auditory space. ***A***, ITD tuning curves (more specifically noise delay functions; black) for input trains of 250, 500, and 1000 Hz center frequency, a purely excitatory model, and a model with dendrites (both receiving input with 500 Hz center frequency). Tuning curves without distally initiated APs are depicted in red, and tuning curves with only distally initiated APs are depicted in green. Gray bar indicates the physiological range of ITDs for gerbils. ***B***, Fraction of distally initiated APs (D-APs) of the tuning curves from ***A***. ***C***, Fisher information (in kHz^2, stimulus duration 300 ms) of the tuning curves (and the respective distal and AIS parts) from ***A***.

different center frequencies and amplitudes. For a low-frequency input with a center frequency of 250 Hz, the rate of distally initiated APs was highest right at the border between no APs and AIS APs (Fig. $7G_1$,G_2). The orientation of this border was diagonal in amplitude–frequency space and qualitatively matched the AP boundaries from Figure 4 (Fig. $7G_1$). For 1000 Hz, the distribution of AIS APs and distally initiated APs is different (Fig. $7H_1$,H_2). There, the boundary between AP firing and no firing was approximately vertical, indicating that the cell effectively implemented an amplitude threshold being insensitive to the slope of the input current (Fig. $7H_1$). Moreover, for 1000 Hz center frequency, distal AP initiation could no longer be seen as a threshold effect. In fact, after an initial dip for low amplitudes, the overall fraction of distally initiated spikes rose with input amplitude (Fig. 7*H*), which is in line with the dependence of the fraction of distally initiated APs on sodium inactivation from Figure 6.

In conclusion, distal AP initiation seems to have two effects. (1) If the sodium channels were only slightly inactivated, the cell is able to fire in response to smaller stimulus amplitudes than without distal initiation of APs. (2) If the sodium channels are largely inactivated (as in the case of temporally summed high-frequency input), distal AP initiation allows the cell to keep up high firing rates for high-frequency stimuli with large stimulus amplitudes.

Impact of distal AP initiation on ITD coding

The above findings have important consequences for the firing behavior of MSO cells *in vivo*. We simulated ITD tuning functions using our ongoing input paradigm with synaptic conductances derived from bandpass-filtered noise. Mimicking phase-locked auditory activity from the two ears, we split up the synaptic inputs into two channels with distinct temporal disparity for the putative ipsilateral and contralateral excitatory synapses, which, disregarding possible additional cochlear and transmission delays, we interpret as an ITD. We assumed that the cell also received phase-locked inhibitory input from both ears (from the medial and lateral nuclei of the trapezoid body) and used the inhibitory synapses to generate a maximum shift in best ITD (Brand et al., 2002; Leibold and van Hemmen, 2005; Pecka et al., 2008; Leibold, 2010). For bandpass input with a center frequency of 250 and 500 Hz, the contralateral inhibition was advanced compared with excitation by 0.8 ms, whereas the ipsilateral inhibition was delayed with respect to excitation by 0.11 ms. For these low center frequencies of the input, the model generated a rate code of ITD (Fig. $8A_1$,A_2) in which firing at low rates was relatively more supported by distally initiated APs (Fig. $8B_1$,B_2). This becomes obvious if one computes Fisher information as a means to assess the ITD resolution of the neuronal responses (Fig. 8*C*). Fisher information (resolution) is particularly high at the slopes of the tuning curves. In line with the high fractions of distally initiated APs at low firing rates (Fig. 8*B*), distally initiated APs also contribute a particularly large amount of information at these low rate regimes. Although, for the present definition of ITDs, these low rate parts are largely outside the physiological range (Fig. 8, gray bars), they might still become physiologically relevant if additional bilaterally asymmetric cochlear, axonal, or cellular delays exist that shift the tuning curves in parallel to the ITD axis.

To achieve the maximal peak shift for bandpass input with a center frequency of 1000 Hz, we set the contralateral inhibition to lead the excitation by 0.5 ms. The situation was very similar to

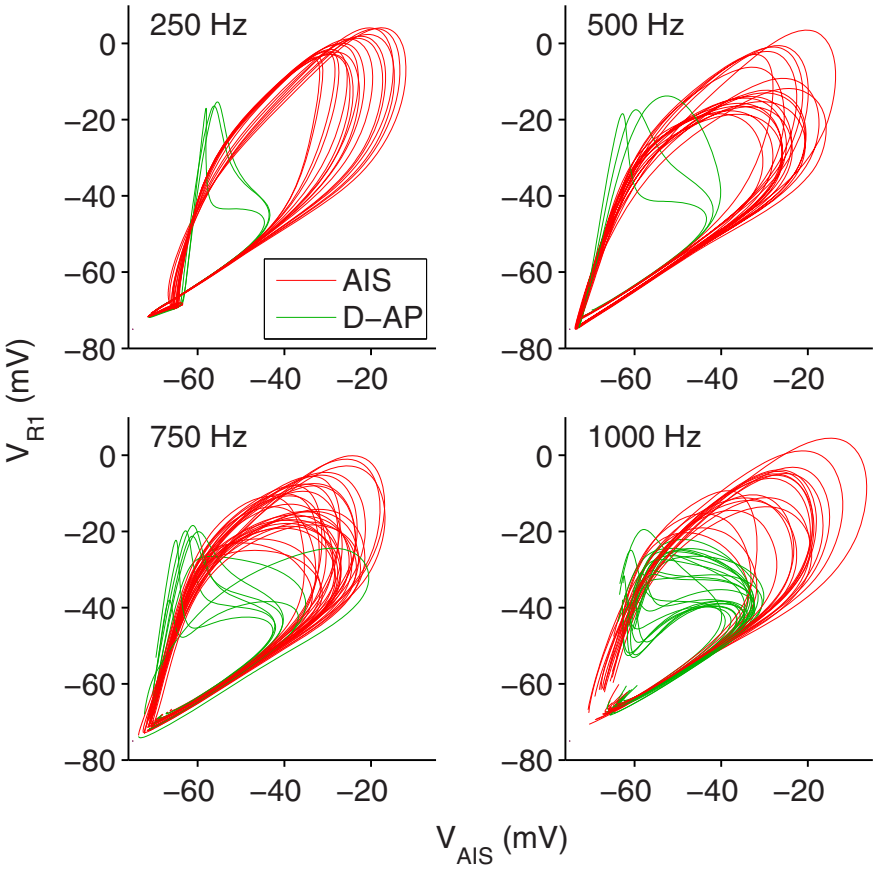

Figure 9. Is there a discrete site of AP initiation? AIS voltage vs voltage at the first node of Ranvier during AP firing for inputs with different center frequencies (as indicated). Red traces are APs identified as AIS APs by the algorithm described in Figure 1*F*. Green traces are APs classified as distally initiated (D-AP).

those for the two lower center frequencies, only that the best ITD, in contrast to *in vivo* findings (Brand et al., 2002), was close to the midline (Fig. 8A_3), and the code was mediated by distal AP initiation to an even larger extent (Fig. 8B_3). Also Fisher information was particularly high for distally initiated APs, even within the physiological range without any additional asymmetric delays (Fig. 8C_3). Thus, the realistically slow decaying inhibition (exponential decay with a time constant of 1.6 ms; Magnusson et al., 2005; Couchman et al., 2010) could well account for the observed peak shifts of low-frequency cells in gerbils, whereas it (at least alone) does not do so for frequencies of ~1 kHz and beyond (Pecka et al., 2008).

As a control, we ran the simulations without inhibitory inputs (Fig. 8A_4,B_4,C_4) which resulted in a best delay of zero. In this case, distally initiated APs were less prevalent. We thus conclude that distal AP initiation is an important mode of AP generation, particularly in the high-frequency channels but also in low-frequency channels with phase-locked inhibition.

In a final set of simulations, we tested how robust our findings are in a model that includes dendrites (Fig. 8A_5,B_5,C_5). MSO neurons typically have two dendrites, a lateral one receives ipsilateral excitatory input fibers and a medial one targeted by contralateral excitatory input fibers. We adjusted the model such that all basic physiological properties matched those of the simpler model and, hence, the published electrophysiological data (Scott et al., 2005; Couchman et al., 2010). The tuning curves and distal AP fractions from this extended model were almost identical to that of the simpler model. We thus conclude that the additional dendritic current sinks do not influence the excitability of the neuron beyond their contribution to the basic physiological parameters (input resistance, resting potential, and EPSP shape).

Discussion

In this study, we used naturalistic synaptic conductance trains to investigate AP initiation in a model of binaural coincidence detector neurons in the MSO, featuring a detailed axonal morphology. Modeling as well as electrophysiology showed that MSO cells incorporate temporal filtering properties such that they were easiest to excite for an input frequency of ~500 Hz. In contrast to current theories, the site of AP generation was not restricted to the AIS but varied depending on the spectral composition of the input. Further distally initiated APs (at the nodes of Ranvier) occurred close to the AP threshold in low-frequency channels, particularly in the presence of inhibition, as well as for strong stimulation in the high-frequency channels. Mechanistically, distal AP initiation at low frequencies was mediated by a strong somatic current sink, whereas for high frequencies it resulted from a stronger sodium channel inactivation in the AIS than in the distal axon. Importantly, in both cases, the ability of the neuron to generate APs in more distal axonal segments increased the dynamic range of firing rates. Distal AP initiation thereby facilitates the resolution of the rate code of ITDs in the cell (Skottun, 1998).

Our model simulations show that AP initiation cannot be viewed to generally occur at one specific site, but rather the proximal axonal segments act as a whole during this process. This is because the axial transport of charge particularly strongly determines the excitability of neighboring axonal segments (Baranauskas et al., 2013). To support the idea of distributed AP generation on a phenomenological level, we compared the trajectories of AIS APs and distally initiated APs plotting AIS voltage against voltage at the first node of Ranvier (Fig. 9). Although, on average, we see a clear distinction between the trajectories of the AIS and distally initiated APs, for higher stimulus frequencies the two sorts of trajectories form a continuum. This means that for some APs it is valid to assign a single site of initiation, but for others (Fig. 9, close to the border between red and green traces) it is rather difficult. A further argument in favor of spatially distributed AP generation is that the distribution of AP initiation sites in our model also depends on stimulus frequency, with high frequencies giving rise to more distal spiking (Fig. 5*I*). This finding is consistent with previous reports about layer 5 pyramidal neurons revealing that the first node of Ranvier facilitates high-frequency (>100 Hz) burst firing and reduces the somatic AP threshold by 5 mV (Kole, 2011). In summary, these results suggest that for high-frequency inputs, AP initiation of MSO cells indeed results from a spatially distributed and collective mechanism,

whereas for low-frequency inputs APs are rather generated at a distinct site.

Our computational model explains the small AP amplitudes observed *in vivo* (Yin and Chan, 1990) and *in vitro* (Scott et al., 2007; Couchman et al., 2010). However, the specific choice of parameters is crucial to further justify the model results. Whereas most of the parameters are closely tied to the existing MSO literature and the new morphometric data presented in this article, specifically the sodium conductances have not yet been determined experimentally in MSO axons. We have set the axonal sodium conductance density such that the firing threshold (70–110 nS) for a single excitatory synaptic conductance stimulus fits our current-clamp measurements (Couchman et al., 2010). Moreover, the axonal sodium conductance density of 4 nS/μm^2 used in the model lies within the range of values reported for cortical pyramidal neuron AISs (2.5 nS/μm^2, Kole et al., 2008) and has been used in several other studies (7.5 nS/μm^2, Shu et al., 2007; 4.5 nS/μm^2, Spirou et al., 2008). In our standard parameter set, we decided to use the same sodium channel density for all unmyelinated axonal compartments (the AIS and the nodes of Ranvier). This simplification rather leads to an underestimation of distal AP initiation (Fig. 5*K*). Assuming a higher sodium channel density in the nodes of Ranvier than in the axon initial segment, as shown by immunogold electron microscopy in cortical pyramidal cells (Lorincz and Nusser, 2010), relatively decreases the excitability of the AIS, thereby increasing the fraction of distally initiated APs.

In the analog ITD circuitry of birds, axonal processing has also been shown to be functionally important (Kuba et al., 2006; Ashida et al., 2007). In NL cells receiving phase-locked inputs up to 3 kHz, the AP initiation zone (clustering of sodium channels) of the AIS is located substantially more distal compared with the low-frequency neurons (Kuba et al., 2006). This finding is in line with the present observation of AP initiation moving to more distal parts of the axon for high-frequency stimuli. Compared with MSO principal neurons, which we suggest to have a dynamically changing site of AP initiation, in NL neurons the site of AP initiation seems rather hardwired, which is also supported by a partial myelination of the initial segment (Carr and Boudreau, 1993).

The mechanisms underlying ITD tuning of MSO principal neurons are highly debated (Grothe et al., 2010; Roberts et al., 2013; van der Heijden et al., 2013). Traditionally, ITD processing was thought to rely exclusively on the coincidence detection of excitatory inputs and neuronal ITD representation on the neurons that respond most at their best ITD. This best ITD is determined by the difference of internal delay lines between the ears and the coincidence detector neuron (Jeffress, 1948). While in the bird systems this concept still seems to constitute the core mechanism underlying ITD maps (Ashida and Carr, 2011), the situation in mammals is less clear. In brainstem and midbrain, the best ITDs change with stimulus frequency inconsistently with the assumption of a solely temporal conduction delay (i.e., they exhibit a so-called characteristic phase; Yin and Chan 1990, Agapiou and McAlpine, 2008, Siveke et al., 2012). Furthermore, blockade of glycinergic transmission *in vivo* shifted the best ITD of MSO neurons toward zero (Brand et al., 2002), hence arguing for a distinct effect of inhibitory inputs on the timing and shape of the excitatory potentials (Brand et al., 2002; Pecka et al., 2008) and providing a putative explanation for the frequency-dependent best ITDs (Leibold, 2010). Although it has been assumed that, given its slow kinetics, inhibition alone cannot account for a substantial shift of the best ITD (Jercog et al., 2010; Day and Semple, 2011; Roberts et al., 2013), our present modeling results show that inhibition has the potential to generate shifts as large as the physiological ITD range of gerbils (~130 μs), at least for frequencies <500 Hz. This, of course, does not exclude further mechanisms like cochlear or axonal delays (Schroeder, 1977; Shamma et al., 1989; Joris et al., 2006; Day and Semple, 2011) and morphological (Zhou et al., 2005; but see Rautenberg et al., 2009) or physiological (Jercog et al., 2010; but see Roberts et al., 2013) asymmetries. A further argument against a contribution of fast inhibition to the shift of best ITDs stems from recent *in vivo* whole-cell recordings (van der Heijden et al., 2013), which state a lack of obvious hyperpolarizing IPSPs. Because of the slow inhibitory time constant, our simulations show that during an ongoing stimulus IPSPs indeed do not show up as isolated potentials (Fig. 1*D*) but nevertheless influence the phase of the monaurally induced oscillations sufficiently to induce a shift of best ITDs (even for 1 kHz, although not much).

Beyond the auditory brainstem, fast and leaky cell membranes have also been reported in cortical pyramidal cells during massive synaptic bombardment such as in high-conductance states [Paré et al., 1998 (who reported input resistances as low as 4 MΩ)] and sharp wave ripple events (Bähner et al., 2011). Under both conditions, the cells show extensive spiking activity *in vivo* (Csicsvari et al., 1999; Steriade, 2001). It is thus tempting to speculate that distal AP initiation contributes to firing as well by allowing the somatic current sink to decouple from the axonal AP-generating zones in a context-dependent manner (Vladimirov et al., 2013).

References

Agapiou JP, McAlpine D (2008) Low-frequency envelope sensitivity produces asymmetric binaural tuning curves. J Neurophysiol 100:2381–2396. CrossRef Medline

Agrawal D, Hawk R, Avila RL, Inouye H, Kirschner DA (2009) Internodal myelination during development quantitated using x-ray diffraction. J Struct Biol 168:521–526. CrossRef Medline

Ashida G, Carr CE (2011) Sound localization: Jeffress and beyond. Curr Opin Neurobiol 21:745–751. CrossRef Medline

Ashida G, Abe K, Funabiki K, Konishi M (2007) Passive soma facilitates submillisecond coincidence detection in the owl's auditory system. J Neurophysiol 97:2267–2282. CrossRef Medline

Bähner F, Weiss EK, Birke G, Maier N, Schmitz D, Rudolph U, Frotscher M, Traub RD, Both M, Draguhn A (2011) Cellular correlate of assembly formation in oscillating hippocampal networks in vitro. Proc Natl Acad Sci U S A 108:E607–616. CrossRef Medline

Baranauskas G, David Y, Fleidervish IA (2013) Spatial mismatch between the Na+ flux and spike initiation in axon initial segment. Proc Natl Acad Sci U S A 110:4051–4056. CrossRef Medline

Baumann VJ, Lehnert S, Leibold C, Koch U (2013) Tonotopic organization of the hyperpolarization-activated current (Ih) in the mammalian medial superior olive. Front Neural Circuits 7:117. CrossRef Medline

Beraneck M, Pfanzelt S, Vassias I, Rohregger M, Vibert N, Vidal PP, Moore LE, Straka H (2007) Differential intrinsic response dynamics determine synaptic signal processing in frog vestibular neurons. J Neurosci 27:4283–4296. CrossRef Medline

Brand A, Behrend O, Marquardt T, McAlpine D, Grothe B (2002) Precise inhibition is essential for microsecond interaural time difference coding. Nature 417:543–547. CrossRef Medline

Carr CE, Boudreau RE (1993) An axon with a myelinated initial segment in the bird auditory system. Brain Res 628:330–334. CrossRef Medline

Couchman K, Grothe B, Felmy F (2010) Medial superior olivary neurons receive surprisingly few excitatory and inhibitory inputs with balanced strength and short-term dynamics. J Neurosci 30:17111–17121. CrossRef Medline

Csicsvari J, Hirase H, Czurkó A, Mamiya A, Buzsáki G (1999) Oscillatory coupling of hippocampal pyramidal cells and interneurons in the behaving Rat. J Neurosci 19:274–287. Medline

Day ML, Semple MN (2011) Frequency-dependent interaural delays in the

medial superior olive: implications for interaural cochlear delays. J Neurophysiol 106:1985–1999. CrossRef Medline

Duflocq A, Chareyre F, Giovannini M, Couraud F, Davenne M (2011) Characterization of the axon initial segment (AIS) of motor neurons and identification of a para-AIS and a juxtapara-AIS, organized by protein 4.1B. BMC Biol 9:66. CrossRef Medline

Ferragamo MJ, Oertel D (2002) Octopus cells of the mammalian ventral cochlear nucleus sense the rate of depolarization. J Neurophysiol 87: 2262–2270. CrossRef Medline

Fitzpatrick DC, Batra R, Stanford TR, Kuwada S (1997) A neuronal population code for sound localization. Nature 388:871–874. CrossRef Medline

Ford MC, Grothe B, Klug A (2009) Fenestration of the calyx of Held occurs sequentially along the tonotopic axis, is influenced by afferent activity, and facilitates glutamate clearance. J Comp Neurol 514:92–106. CrossRef Medline

Foust A, Popovic M, Zecevic D, McCormick DA (2010) Action potentials initiate in the axon initial segment and propagate through axon collaterals reliably in cerebellar Purkinje neurons. J Neurosci 30:6891–6902. CrossRef Medline

Gentet LJ, Stuart GJ, Clements JD (2000) Direct measurement of specific membrane capacitance in neurons. Biophys J 79:314–320. CrossRef Medline

Glasberg BR, Moore BC (1990) Derivation of auditory filter shapes from notched-noise data. Hear Res 47:103–138. CrossRef Medline

Goldberg JM, Brown PB (1969) Response of binaural neurons of dog superior olivary complex to dichotic tonal stimuli: some physiological mechanisms of sound localization. J Neurophysiol 32:613–636. Medline

Golding NL, Oertel D (2012) Synaptic integration in dendrites: exceptional need for speed. J Physiol 590:5563–5569. CrossRef Medline

Grothe B, Pecka M, McAlpine D (2010) Mechanisms of sound localization in mammals. Physiol Rev 90:983–1012. CrossRef Medline

Jeffress LA (1948) A place theory of sound localization. J Comp Physiol Psychol 41:35–39. CrossRef Medline

Jercog PE, Svirskis G, Kotak VC, Sanes DH, Rinzel J (2010) Asymmetric excitatory synaptic dynamics underlie interaural time difference processing in the auditory system. PLoS Biol 8:e1000406. CrossRef Medline

Joris PX, Van de Sande B, Louage DH, van der Heijden M (2006) Binaural and cochlear disparities. Proc Natl Acad Sci U S A 103:12917–12922. CrossRef Medline

Kapfer C, Seidl AH, Schweizer H, Grothe B (2002) Experience-dependent refinement of inhibitory inputs to auditory coincidence-detector neurons. Nat Neurosci 5:247–253. CrossRef Medline

Koch U, Braun M, Kapfer C, Grothe B (2004) Distribution of HCN1 and HCN2 in rat auditory brainstem nuclei. Eur J Neurosci 20:79–91. CrossRef Medline

Kole MH (2011) First node of Ranvier facilitates high-frequency burst encoding. Neuron 71:671–682. CrossRef Medline

Kole MH, Letzkus JJ, Stuart GJ (2007) Axon initial segment Kv1 channels control axonal action potential waveform and synaptic efficacy. Neuron 55:633–647. CrossRef Medline

Kole MH, Ilschner SU, Kampa BM, Williams SR, Ruben PC, Stuart GJ (2008) Action potential generation requires a high sodium channel density in the axon initial segment. Nat Neurosci 11:178–186. CrossRef Medline

Kuba H, Ishii TM, Ohmori H (2006) Axonal site of spike initiation enhances auditory coincidence detection. Nature 444:1069–1072. CrossRef Medline

Leibold C (2010) Influence of inhibitory synaptic kinetics on the interaural time difference sensitivity in a linear model of binaural coincidence detection. J Acoust Soc Am 127:931–942. CrossRef Medline

Leibold C, van Hemmen JL (2005) Spiking neurons learning phase delays: how mammals may develop auditory time-difference sensitivity. Phys Rev Lett 94:168102. CrossRef Medline

Lorincz A, Nusser Z (2010) Molecular identity of dendritic voltage-gated sodium channels. Science 328:906–909. CrossRef Medline

Magnusson AK, Kapfer C, Grothe B, Koch U (2005) Maturation of glycinergic inhibition in the gerbil medial superior olive after hearing onset. J Physiol 568:497–512. CrossRef Medline

Mainen ZF, Sejnowski TJ (1996) Influence of dendritic structure on firing pattern in model neocortical neurons. Nature 382:363–366. CrossRef Medline

Mainen ZF, Joerges J, Huguenard JR, Sejnowski TJ (1995) A model of spike initiation in neocortical pyramidal neurons. Neuron 15:1427–1439. CrossRef Medline

Mathews PJ, Jercog PE, Rinzel J, Scott LL, Golding NL (2010) Control of submillisecond synaptic timing in binaural coincidence detectors by K(v)1 channels. Nat Neurosci 13:601–609. CrossRef Medline

McIntyre CC, Richardson AG, Grill WM (2002) Modeling the excitability of mammalian nerve fibers: influence of afterpotentials on the recovery cycle. J Neurophysiol 87:995–1006. Medline

McIntyre CC, Grill WM, Sherman DL, Thakor NV (2004) Cellular effects of deep brain stimulation: model-based analysis of activation and inhibition. J Neurophysiol 91:1457–1469. CrossRef Medline

Palmer LM, Stuart GJ (2006) Site of action potential initiation in layer 5 pyramidal neurons. J Neurosci 26:1854–1863. CrossRef Medline

Palmer LM, Clark BA, Gründemann J, Roth A, Stuart GJ, Häusser M (2010) Initiation of simple and complex spikes in cerebellar Purkinje cells. J Physiol 588:1709–1717. CrossRef Medline

Paré D, Shink E, Gaudreau H, Destexhe A, Lang EJ (1998) Impact of spontaneous synaptic activity on the resting properties of cat neocortical pyramidal neurons In vivo. J Neurophysiol 79:1450–1460. Medline

Pecka M, Brand A, Behrend O, Grothe B (2008) Interaural time difference processing in the mammalian medial superior olive: the role of glycinergic inhibition. J Neurosci 28:6914–6925. CrossRef Medline

Popovic MA, Foust AJ, McCormick DA, Zecevic D (2011) The spatiotemporal characteristics of action potential initiation in layer 5 pyramidal neurons: a voltage imaging study. J Physiol 589:4167–4187. CrossRef Medline

Rautenberg PL, Grothe B, Felmy F (2009) Quantification of the three-dimensional morphology of coincidence detector neurons in the medial superior olive of gerbils during late postnatal development. J Comp Neurol 517:385–396. CrossRef Medline

Roberts MT, Seeman SC, Golding NL (2013) A mechanistic understanding of the role of feedforward inhibition in the mammalian sound localization circuitry. Neuron 78:923–935. CrossRef Medline

Rothman JS, Manis PB (2003) The roles potassium currents play in regulating the electrical activity of ventral cochlear nucleus neurons. J Neurophysiol 89:3097–3113. CrossRef Medline

Schroeder MR (1977) New viewpoints in binaural interactions. In: Psychophysics and physiology of hearing (Evans EF, Wilson JP, eds), pp 455–467. New York: Academic.

Scott LL, Mathews PJ, Golding NL (2005) Posthearing developmental refinement of temporal processing in principal neurons of the medial superior olive. J Neurosci 25:7887–7895. CrossRef Medline

Scott LL, Hage TA, Golding NL (2007) Weak action potential backpropagation is associated with high-frequency axonal firing capability in principal neurons of the gerbil medial superior olive. J Physiol 583:647–661. CrossRef Medline

Scott LL, Mathews PJ, Golding NL (2010) Perisomatic voltage-gated sodium channels actively maintain linear synaptic integration in principal neurons of the medial superior olive. J Neurosci 30:2039–2050. CrossRef Medline

Shamma SA, Shen NM, Gopalaswamy P (1989) Stereausis: binaural processing without neural delays. J Acoust Soc Am 86:989–1006. CrossRef Medline

Shu Y, Duque A, Yu Y, Haider B, McCormick DA (2007) Properties of action-potential initiation in neocortical pyramidal cells: evidence from whole cell axon recordings. J Neurophysiol 97:746–760. CrossRef Medline

Siveke I, Leibold C, Schiller E, Grothe B (2012) Adaptation of binaural processing in the adult brainstem induced by ambient noise. J Neurosci 32: 462–473. Medline

Skottun BC (1998) Sound location and neurons. Nature 393:531. CrossRef Medline

Spirou GA, Chirila FV, von Gersdorff H, Manis PB (2008) Heterogeneous Ca2+ influx along the adult calyx of held: a structural and computational study. Neuroscience 154:171–185. CrossRef Medline

Steriade M (2001) Impact of network activities on neuronal properties in corticothalamic systems. J Neurophysiol 86:1–39. Medline

Stuart GJ, Sakmann B (1994) Active propagation of somatic action poten-

tials into neocortical pyramidal cell dendrites. Nature 367:69–72. CrossRef Medline

Stuart G, Schiller J, Sakmann B (1997) Action potential initiation and propagation in rat neocortical pyramidal neurons. J Physiol 505:617–632. CrossRef Medline

Svirskis G, Kotak V, Sanes DH, Rinzel J (2002) Enhancement of signal-to-noise ratio and phase locking for small inputs by a low-threshold outward current in auditory neurons. J Neurosci 22:11019–11025. Medline

van der Heijden M, Lorteije JA, Plauška A, Roberts MT, Golding NL, Borst JG (2013) Directional hearing by linear summation of binaural inputs at the medial superior olive. Neuron 78:936–948. CrossRef Medline

Vladimirov N, Tu Y, Traub RD (2013) Synaptic gating at axonal branches, and sharp-wave ripples with replay: a simulation study. Eur J Neurosci 38:3435–3447. CrossRef Medline

Werthat F, Alexandrova O, Grothe B, Koch U (2008) Experience-dependent refinement of the inhibitory axons projecting to the medial superior olive. Dev Neurobiol 68:1454–1462. CrossRef Medline

Yin TC, Chan JC (1990) Interaural time sensitivity in medial superior olive of cat. J Neurophysiol 64:465–488. Medline

Zhou Y, Carney LH, Colburn HS (2005) A model for interaural time difference sensitivity in the medial superior olive: interaction of excitatory and inhibitory synaptic inputs, channel dynamics, and cellular morphology. J Neurosci 25:3046–3058. CrossRef Medline